1   **The evolution of biomass-burning aerosol size distributions due to**

2   **coagulation: dependence on fire and meteorological details and**

3   **parameterization**

5   **K.M. Sakamoto[1], R.G. Stevens[2] and J. R. Pierce[1,3]**

7   [1] Colorado State University, Fort Collins, CO, USA

8   [2] University of Leeds, Leeds, UK

9   [3] Dalhousie University, Halifax, NS, Canada

11   Corresponding author: J.R. Pierce (jeffrey.pierce@colostate.edu)

Abstract

14   Biomass-burning aerosols have a significant effect on global and regional aerosol climate forcings. To

15   model the magnitude of these effects accurately requires knowledge of the size distribution of the

16   emitted and evolving aerosol particles. Current biomass-burning inventories do not include size

17   distributions, and global and regional models generally assume a fixed size distribution from all

18   biomass-burning emissions. However, biomass-burning size distributions evolve in the plume due to

19   coagulation and net organic aerosol (OA) evaporation or formation, and the plume processes occur on

20   spacial scales smaller than global/regional-model grid boxes. The extent of this size-distribution

21   evolution is dependent on a variety of factors relating to the emission source and atmospheric

22   conditions. Therefore, to account for biomass-burning aerosol size in global models accurately requires

23   an *effective* aerosol size distribution that accounts for this sub-grid evolution and can be derived from

24   available emissions-inventory and meteorological parameters.

25   In this paper, we perform a detailed investigation of the effects of coagulation on the aerosol size

26   distribution in biomass-burning plumes. We compare the effect of coagulation to that of OA

27   evaporation and formation. We develop coagulation-only parameterizations for effective

28   biomass-burning size distributions using the SAM-TOMAS large-eddy simulation plume model. For

29   the most-sophisticated parameterization, we use the Gaussian Emulation Machine for Sensitivity

30 Analysis (GEM-SA) to build a parameterization of the aged size distribution based on the

31 SAM-TOMAS output and seven inputs: emission median dry diameter, emission distribution modal

32 width, mass emissions flux, fire area, mean boundary-layer wind speed, plume mixing depth, and

33 time/distance since emission. This parameterization was tested against an independent set of

34 SAM-TOMAS simulations, and yields R^2 values of 0.83 and 0.89 for D_{pm} and modal width,

35 respectively. The aged size distribution is particularly sensitive to the mass emissions flux, fire area,

36 wind speed, and time, and we provide simplified fits of the aged size distribution to just these input

37 variables. These fits may be used in global and regional aerosol models. Finally, we show that

38 variability in coagulation may lead to greater variability in the particle size distribution than does OA

39 evaporation/formation using estimates of OA production/loss from the literature.

1. Introduction

40

1.1 Biomass-burning aerosols

41

42 Biomass burning (including wildfires, prescribed fires, and agricultural fires) releases significant

43 amounts of gas- and particle-phase species to the atmosphere (Andreae and Merlet, 2001; Reid et al.,

44 2005). The particle-phase emissions are composed primarily of a mixture of organic aerosol (OA) and

45 black carbon (BC) with some inorganic species (e.g. potassium), and the ratios of these species depend

46 on the source fire conditions (Capes et al., 2008; Carrico et al., 2010; Cubison et al., 2011; Hecobian et

47 al., 2011; Hennigan et al., 2011; Reid et al., 2005). These aerosols affect the global radiation budget

48 through the indirect and direct aerosol effects (Boucher et al., 2013). The smoke particles themselves

49 are able to act as cloud condensation nuclei (CCN) and increase cloud albedo and lifetime (indirect

50 aerosol effect; Lee et al., 2013; Pierce et al., 2007; Spracklen et al., 2011) as well as

51 scattering/absorbing incoming solar-radiation directly (direct aerosol effect; Alonso-Blanco et al.,

52 2014; Boucher et al., 2013; Haywood and Boucher, 2000; Jacobson, 2001).

53   Particle size has a significant effect on the magnitude of both the direct and indirect aerosol

54 effects (Lee et al., 2013; Seinfeld and Pandis, 2006; Spracklen et al., 2011). The composition and

55 diameter of the particles affect their absorption/scattering efficiencies, which dictate the amount of

56 solar radiation absorbed/scattered per emitted mass of particles (Seinfeld and Pandis, 2006). Particle

57 diameter and hygroscopicity determine the particles' ability to act as a CCN and influence cloud

58 processes, and the total number of emitted particles increases with decreased particle size if total mass

59   emissions are fixed. Spracklen et al., (2011) found that a reduction by a factor of two in particle size for

60   all carbonaceous aerosols (for a fixed total aerosol mass) resulted in a ~300% increase in the cloud

61   albedo indirect effect globally, as more particles were available to act as CCN. Lee et al., (2013)

62   determined that CCN concentrations in the GLOMAP model were very sensitive to uncertainties in

63   biomass-burning emission diameter on both the regional and global scale (its attributable CCN

64   uncertainty ranked third of 28 factors tested globally). Therefore, to ascertain the role of

65   biomass-burning aerosols in climate forcings accurately, biomass-burning size distributions must be

66   well represented in aerosol-climate models.

67   Size distributions are subject to physical and chemical processing in the plume. The formation of

68   secondary organic aerosol (SOA) has been observed in lab studies of biomass-burning aerosol

69   (Cubison et al., 2011; Grieshop et al., 2009; Hennigan et al., 2011; Heringa et al., 2011; Ortega et al.,

70   2013) and in field campaigns (DeCarlo et al., 2010; Lee et al., 2008; Reid et al., 1998; Yokelson et al.,

71   2009). This SOA condenses onto existing particles causing growth of the aerosol size distribution.

72   Conversely, recent lab and field studies have characterized primary organic aerosol (POA) as

73   semi-volatile, with plume dilution allowing the evaporation of organic aerosol from particles (Huffman

74   et al., 2009; Cubison et al., 2011; May et al., 2013,). The cumulative net effects of OA production/loss

75   within biomass-burning plumes has been found to be highly variable from fire to fire (Hennigan et. al,

76   2011). Coagulation is also important for size-distribution evolution as it reduces particle number and

77   shifts the distribution to larger sizes. Coagulation rates are proportional to the square of the particle

78   number concentration (all else remaining fixed), so the high number concentrations in biomass-burning

79   plumes relative to background can lead to rapid coagulational growth of the size distribution. The rate

80   and magnitude of the aerosol growth caused by these combined processes is a function of aging time,

81   emission source characteristics, aerosol properties at emission, and atmospheric conditions.

82   These condensation/evaporation and coagulation aging processes affect both the composition and

83   size of the aerosol size distribution – both properties that influence the extent to which smoke particles

84   affect climate. While fresh smoke is generally composed of fine particles between 20-60 nm in

85   diameter (Levin et al., 2010), condensation and coagulation cause rapid aerosol growth to larger sizes

86   (over 100 nm) on timescales of often less than 24 hrs (Janhäll et al., 2010). However, Janhäll et al.,

87   (2010) found the observed geometric mean diameter of aged biomass-burning particles varied between

88   170-300 nm, with geometric standard deviations (hereafter referred to as "modal width") between

89   1.3-1.7 with significant dependence on fuel type and modified combustion efficiency. It is currently

90   unclear to what extent these factors and others drive the variability in aged size distributions.

91   As stated earlier, an accurate representation of aged biomass-burning aerosol size is necessary for

92   predictions of aerosol climate effects in regional and global models (Lee et al., 2013). Current wildfire

93   inventories are mass-based (neglecting aerosol size data), and thus regional and global models used for

94   aerosol-climate effects generally specify fixed, "aged" size distributions that do not account for

95   sub-grid processing of the emitted particles (Reid et al., 2009; van der Werf et al., 2010; Wiedinmyer et

96   al., 2011). Any variability in the biomass-burning size distribution due to fire or emissions

97   characteristics and meteorology are not accounted for, nor is it clear what the best "aged" size

98   distribution to use is in these models.

99   In this paper, we perform a detailed investigation of coagulation in biomass-burning plumes and

100 compare to the effects of OA evaporation and formation. We investigate the factors that influence

101 coagulational growth of the particles in the plume. These factors include fire area, particle-emissions

102 mass flux, particle-emissions size, and meteorological conditions. We create parameterizations of

103 varying degrees of complexity for median dry diameter (D_{pm}) and lognormal modal width (σ) of the

104 aged biomass-burning size distributions as a function of these input parameters, based on detailed

105 numerical simulations using a large-eddy model with embedded aerosol microphysics (SAM-TOMAS).

106 Finally, we compare the effect of coagulation on the aerosol size distribution to that of OA

107 production/evaporation.

108   We describe the parameterization building process, including the use of a Gaussian emulator, in

109 Sect. 2. A discussion of input and output ranges, processing, and constraints of the parameters we have

110 chosen is provided in Sect. 2.1. We discuss the SAM-TOMAS model and the emulation process in Sect.

111 2.2-2.3. Sections 3.1-3.2 contain the results of the SAM-TOMAS model and the emulator. We discuss

112 emulator sensitivities to the inputs in Sect. 3.3 and present a series of simplified fit equations for the

113 effective size distributions in Sect. 3.4. We discuss the effects of potential OA production/loss on our

114 size distribution estimates in Sect. 3.5. Finally, we conclude in Sect. 4, including future plans for testing

115 the parameterization and known existing limitations.

116

117

2. Methods

118

119 Figure 1 provides an overview of our methods that will be described in detail in the subsections below.

120 In short, we used a Large-Eddy Simulation model, the System for Atmospheric Modelling (SAM;

121 Khairoutdinov and Randall, 2003), with the online aerosol microphysics module, TwO Moment

122 Aerosol Sectional (TOMAS, Adams and Seinfeld, 2002; Stevens et al., 2012) to simulate the evolution

123 of the biomass-burning aerosol size distribution by coagulation across a wide range of emission and

124 meteorological conditions. We used the SAM-TOMAS size distributions to build parameterizations to

125 predict aged D_{pm} and σ using: (1) a statistical emulator of the SAM-TOMAS model itself and (2)

126 simplified fits to the SAM-TOMAS output data. The statistical emulator was built by the Gaussian

127 Emulation Machine for Sensitivity Analysis (GEM-SA), and we used the emulator and SAM-TOMAS

128 data to determine the relative importance of various inputs to shaping the aged size distribution.

2.1 Investigated factors that may lead to variability in aged size distributions

129

130 We investigated seven parameters that may affect the aging of the biomass-burning aerosol size

131 distribution. These can be divided into those representing the initial lognormal-mode size parameters

132 (D_{pm0}, σ_0), fire conditions (mass flux, fire area), atmospheric conditions (wind speed, plume mixing

133 depth), and time. Each of these parameters is generally available in large-scale aerosol models, which

134 means a parameterization for aged biomass-burning size distributions based on these parameters may

135 be used in these models. Table 1 lists these input parameters and the ranges of values tested in this

136 work.

137 We assumed that the initial size distributions were a single lognormal mode (described by dry

138 median diameter, D_{pm}, and modal width, σ), which is sufficient when representing both fresh and aged

139 observed biomass-burning size distributions (Capes et al., 2008; Janhäll et al., 2010; Levin et al., 2010;

140 Sakamoto et al., 2015). The initial size-distribution parameters specify the median dry diameter (D_{pm0})

141 and modal width (σ_0) of the freshly emitted aerosol distribution. We varied these parameters between

142 20-100 nm for D_{pm0} and 1.2-2.4 for σ_0. The large ranges are due to variability in combustion efficiency

143 and fuel-type factors as seen in lab and observational studies (Janhäll et al., 2010; Levin et al., 2010).

144 Fire area, mass flux, wind speed and mixing depth (the vertical extent of the aerosol plume) all

145 affect the aerosol number concentration (N) within the plume, which in turn affects the coagulation rate

146 (proportional to N^2). In our simulations, we constrained mass flux to 2 x 10^{-8} - 5 x 10^{-6} kg m^{-2} s^{-1} using

147 approximate maximum and minimum values of summed black carbon and organic carbon flux

148 (BC+OC) found in the Global Fire Emissions Database ver. 3 (GFED3; van der Werf et al., 2010;

149 available from http://www.globalfiredata.org). Fire area ranged from 1 - 49 km^2 (simulated as a square),

150 which was found to represent the range of fire sizes in GFED3. Boundary layer wind speed varied

151 between 2 m s^{-1} and 20 m s^{-1} and was based on ranges in the National Center for Environmental

152 Prediction (NCEP) North American Regional Reanalysis (NARR) meteorology (Mesinger et al., 2006)

153 during the fire season (specifically, July, 2010). Mixing depth had a range of 150-2500 m (based on

154 SAM-TOMAS output; see Sect. 2.2).

155   The aging time was the final input parameter, and we used 5 hr (300 min) as an upper time

156 bound due to this being a typical timescale for transport across large global model gridboxes.

2.2 The SAM-TOMAS model

157

158 We used the SAM-TOMAS model to simulate the evolution of biomass-burning aerosol size

159 distributions due to coagulation across the range of input parameters described above. SAM

160 (Khairoutdinov and Randall, 2003) is a dynamical large-eddy simulation (LES) model, which has

161 previously been used to model emissions plumes (Lonsdale et al., 2012; Stevens et al., 2012; Stevens

162 and Pierce, 2013). We ran the model in Lagrangian 2D mode (Stevens and Pierce, 2013), in which a

163 wall oriented normal to the mean boundary layer wind moves at the mean boundary-layer wind speed.

164 This moving wall tracks the radial dispersion of a plume as it travels downwind (Fig. 2). This 2D mode

165 is computationally efficient compared to the full 3D model with minor differences due to axial plume

166 symmetry (Stevens and Pierce, 2013).

167   The size distributions of the aerosol particles in SAM were simulated using the TwO Moment

168 Aerosol Sectional (TOMAS; Adams and Seinfeld, 2002) microphysical scheme embedded into SAM.

169 The algorithm simulated the size distribution across 15 logarithmically-spaced size bins spanning 3

170 nm-10 μm. The aerosol size distribution was tracked via two independent moments for each bin of the

171 size distribution (mass and number). TOMAS calculated coagulation explicitly in each grid cell

172 assuming a Brownian diffusion kernel (Seinfeld and Pandis, 2006). Our SAM-TOMAS simulations

173 included only coagulation, and particles were assumed to be a single species (no differentiating

174 between BC and OA). The SAM-TOMAS model had previously been tested against observations in

175   Stevens et al. (2012) and Lonsdale et al. (2012) for power plant plumes.

176   We set background aerosol concentrations to zero as the biomass-burning aerosol

177   concentrations emitted into SAM-TOMAS were orders of magnitude larger than those present in a

178   remote background location, and as such the lack of background aerosol would have had an

179   insignificant effect on the rate of in-plume coagulational processing. The biomass-burning aerosol was

180   assumed to have a constant density of 1400 kg m^{-3} as primarily a mix of organic compounds, thus we

181   do not consider how changes in BC/OA composition may affect density and coagulation rates. The

182   hygroscopicity of the aerosol particles was set to zero, allowing no water uptake. This assumption is

183   not true of real world biomass-burning aerosol and has been characterized in other works finding

184   hygroscopicities of fresh (κ=0.02-0.8; Petters et al., 2009) and aged smoke (κ=0.1-0.3; Engelhart et al.,

185   2012) with a strong dependence on fuel type. In terms of their effect on the size distribution, a constant

186   κ across all particle sizes has the simple effect of increasing the effective diameter of the particles via

187   water uptake by a scalar factor. This initial increase should only have a relatively minor effect on the

188   final dry D_{pm} or σ of the plume after coagulational processing as the mean coagulation rates are

189   relatively insensitive to the size shifting of a particle population (Seinfeld and Pandis, 2006; Stuart et

190   al., 2013).

191   We ran 100 SAM-TOMAS simulations at 500 m x 500 m horizontal resolution (total horizontal

192   extent = 100 km), and constant 40 m vertical resolution (total vertical extent = 4 km). This resolution

193   accommodated the chosen plume parameters (see Sect. 2.1). The model was run with a master timestep

194   of 2 seconds (varied internally for accuracy in the coagulation calculation) for a duration of 5 model

195   hours (300 minutes). The output from each SAM-TOMAS simulation was recorded at four different

196   times (400 total time slices across 100 simulations).

197   The seven inputs to the SAM-TOMAS model were constrained to capture a range of

198   biomass-burning characteristics in realistic scenarios and are summarized in Table 2. The ranges of

199   values used for D_{pm0}, σ_0, fire area and mass flux are the same as those listed in Table 1. The

200   meteorological fields were supplied by NCEP reanalysis meteorology from over North America (land

201   only, lat: 30º - 70º N, lon: 70º -135º W) during the July 2010 fire season. The SAM-TOMAS wall speed

202   was set equal to the mean boundary layer wind speed from NCEP. We filtered these inputs by requiring

203   wind speed > 2 m s^{-1} to eliminate stagnation situations over the source. The injection height (lower

204   bound) and injection depth of the aerosol were specified at between 50-1500 m and 500-2000 m

205   respectively. No emission injection parameterization (e.g. Freitas et al., 2007) was used as we were

206 only trying to capture a range of mixing depths for our aging calculation, and the absolute height was

207 relatively unimportant. All the SAM-TOMAS simulation inputs were chosen using semi-random Latin

208 hypercube sampling across the ranges listed above (Lee et al., 2012). The results of the full

209 SAM-TOMAS simulation set are summarized in Sect. 3.1.

210 We calculated the time-dependent mixing depth of the plume from vertical profiles averaged

211 horizontally across the entire simulation wall at each time slice. Figure 3 shows a sample of six vertical

212 profiles from different SAM-TOMAS simulations. The mixing depth was defined as the range of

213 altitudes where the aerosol mass was greater than half of the peak aerosol mass:

214
$$\text{mixing depth} = \Delta_{\text{alt 50\% peak aerosol mass}}$$

215 In cases where the plume mixed down to the ground, the lower altitude bound was defined as 0

216 m. Runs with mixing depths greater than 2500 m were excluded to ensure that the plume did not reach

217 the model top. In addition to mixing depth, D_{pm} and σ were calculated for each of the SAM-TOMAS

218 time slices from the first and third integrated moments of the size distribution as detailed by Whitby et

219 al. (1991).

2.3 Emulation of the SAM-TOMAS output

220

221 As running the full SAM-TOMAS model is too computationally expensive for implementation in

222 global aerosol models, we built an offline emulator of the model for use as a parameterization in these

223 global models. We created the emulator using the Gaussian Emulation Machine for Sensitivity Analysis

224 (GEM-SA) developed by the Centre for Terrestrial Dynamics (http://www.ctcd.group.shef.ac.uk/gem.html).

225 The GEM-SA software uses a Gaussian process to design a SAM-TOMAS simulator (the emulator)

226 based on the behavior of the known SAM-TOMAS inputs and outputs (the training data). A complete

227 description of GEM-SA statistics and assumptions can be found in Kennedy and O'Hagan (2001) and

228 Kennedy et al. (2008). A description of its application as an estimator in atmospheric-aerosol modelling

229 can be found in Lee et al. (2011). This software was previously used in sensitivity studies in

230 atmospheric-aerosol (Lee et al., 2011, 2012) and vegetation models (Kennedy et al., 2008).

231 We used 400 data points from the set of 100 SAM-TOMAS simulations to train the emulator.

232 GEM-SA assumes that the outputs are a continuous and differentiable function of the inputs to

233 statistically emulate the model and estimate the SAM-TOMAS output (D_{pm} and σ). We used a new set

234   of completed SAM-TOMAS simulations (624 non-training data points) to test our GEM-SA

235   parameterization for accuracy relative to SAM-TOMAS (see Sect. 3.2-3.3).

236   The GEM-SA parameterization requires seven input parameters: D_{pm0}, σ_0, mass flux, fire area,

237   wind speed, mixing depth and time, and generates predicted aged D_{pm} and σ as outputs. These

238   estimated D_{pm} and σ describe an aged lognormal aerosol mode incorporating the sub-grid scale

239   coagulation taking place inside concentrated biomass-burning plumes and can be used in

240   global/regional models. We have made the GEM-SA parameterization (emulator Fortran subroutine and

241   input files) available as Supplementary Material.

242   3. Results

243   *3.1 SAM-TOMAS simulation output*

244   Figure 4 shows the D_{pm} (panels a and c) and σ (panels b and d) as a function of distance for each of the

245   100 SAM-TOMAS simulations used to train the emulator (Sect. 3.2). The influence of several factors

246   (the distance from the source, emissions mass flux, and fire area) on the final aerosol size distributions

247   is apparent in the output of SAM-TOMAS simulations. Panels a and b are colored by the emissions

248   mass flux, whereas panels c and d are colored by dM/dx (kg m^{-1}, the amount of aerosol mass in an

249   infinitesimally thin slice of air perpendicular to the direction of the wind, i.e. mass flux · fire area /

250   wind speed). All simulations showed D_{pm} increasing with distance as coagulation progressed in each

251   plume. The coloring in panel a shows that D_{pm} generally increases more rapidly and to higher values

252   with higher emission fluxes. However, panel c shows that dM/dx appears to be a better predictor for the

253   increase of D_{pm} with distance than the emissions flux, and the distance and dM/dx capture much of the

254   variability in D_{pm}. D_{pm0} appears to have little influence on D_{pm} (note, however, that the first points on

255   these plots already include some processing and are not the initial diameters).

256   Panels b and d show that σ tends to converge with distance as simulations with large initial σ

257   generally decrease with distance more rapidly than simulations with smaller initial σ. This convergence

258   happens slowly relative to the times simulated, so the initial σ have a strong influence even at 200 km.

259   The colors and panels b and d show that σ in high emissions-flux and dM/dx cases converge more

260   rapidly than low-emissions cases. However, as opposed to the 1.32 modal-width asymptote in the limit

261   of infinite coagulation found by Lee (1983), the SAM-TOMAS simulations converge to a limit of

262   1.2-1.25. This is likely due to the size-distribution bin-spacing in the SAM-TOMAS model, where

263   modal widths <1.32 are smaller than a single TOMAS size bin width, which results in less accurate fits

264   of σ for smaller σ values.

265   Figure 5 is a scatterplot of D_{pm} vs σ for each point seen in Fig. 4, excepting those at distances

266   less than 25 km (points close to the emissions source have been removed). The points are colored by

267   dM/dx. Thus, Fig. 5 shows the results of Fig. 4 panels c and d together but removes the distance

268   information. At these distances over 25 km, D_{pm} is relatively well constrained by dM/dx alone, showing

269   that the mean growth by coagulation is strongly influenced by the mass of particles in the slice of air.

270   On the other hand, σ is unconstrained at low values of dM/dx but more constrained towards 1.2-1.4 at

271   high values of dM/dx. At high dM/dx values, the convergence towards the steady-state σ proceeds

272   much more rapidly than at low dM/dx as also shown in Fig. 4d.

273   These SAM-TOMAS results show that dM/dx is a powerful determinant of aged

274   biomass-burning size. In these tests, we also explored dividing dM/dx by the final mixing depth to

275   create dM/dxdz (mass flux · fire area / wind speed / mixing depth). Large mixing depths dilute particle

276   concentrations and reduce coagulation, so we expected that dM/dxdz may be a better predictor of

277   biomass-burning size-distribution aging than dM/dx. However, Fig. 4 and Fig. 5 did not look

278   qualitatively different when using dM/dxdz. We quantitatively evaluate the fidelity of dM/dx and

279   dM/dxdz as proxies for biomass-burning size-distribution aging in Sect. 3.4. In the following two

280   subsections, we use the emulator to determine the contribution of the individual inputs to the changes

281   in simulated D_{pm} and σ.

3.2 Model parameterization evaluation

283   We tested the GEM-SA-derived emulator parameterization against additional SAM-TOMAS model

284   runs that were not used in the fitting of the parameterization, and we show the results in Fig. 6. We use

285   624 additional SAM-TOMAS-simulated data points that were not used for GEM-SA training in this

286   evaluation. The emulator parameterization-predicted outputs corresponding to these data points for D_{pm}

287   and σ are plotted against the SAM-TOMAS D_{pm} and σ. Predicted D_{pm} has an R^2 value of 0.83 with a

288   slope of 0.92. Larger absolute errors in D_{pm} are found at the larger diameter sizes, but 86% are found

289   within 10% of the SAM-TOMAS D_{pm} (76% of predicted D_{pm} are within 5% of SAM-TOMAS D_{pm}).

290   The small mean normalized bias (MNB) of -0.06 indicates a slight negative bias in the

291   parameterization. This bias is generally seen towards the higher final D_{pm} values in the simulations

292   (>250 nm), which are reached only by the most aged plumes with the heaviest aerosol loads. The σ plot

293   (Fig. 6b) shows a similar correlation coefficient (R^2=0.91) and has a slope of 0.93. The MNB is 0.01

294   and 77% of the predicted σ points are within 5% of the σ calculated from SAM-TOMAS. The cluster of

295   points near σ =1.2-1.3 is indicative of the modal width steady-state limit. This limit is not captured by

296   the σ parameterization, which assumes a smooth function towards even lower σ values.

3.3 Sensitivity of aged size distribution to input parameters

297

298   Figures 7 and 8 show the sensitivities of the parameterization outputs (D_{pm} and σ, respectively) to the

299   input parameters (D_{pm0}, σ_0, mass flux, fire area, wind speed, time, and mixing depth) as determined by

300   the GEM-SA emulation of the SAM-TOMAS output. (Note that distance was used as the dependent

301   variable in Fig. 4, while we use time in the emulator. Time can be converted to distance by multiplying

302   by the wind speed). In every panel, each line shows the change in D_{pm} (Fig. 7) or σ (Fig. 8) as an input

303   parameter (e.g. D_{pm0} in panel a) is varied systematically from its minimum to maximum tested value

304   with a randomly chosen set of the other six input parameters. Each panel contains 100 lines, which

305   means that 100 sets of the six other input parameters were randomly chosen to make these lines. We

306   normalize each line by the value of D_{pm} or σ at the midpoint of the x-axis (i.e. where the input

307   parameter is at the midpoint of its tested range). For time since emission (panel f) we normalize by the

308   values at t=0 min instead of at the midpoint of the range. These plots therefore show the percent change

309   in D_{pm} or σ, $\Delta\%_{output}$, as each input is changed from its midpoint value (or t=0 min for time), in order to

310   emphasize the parameterization's output response to each isolated input variable.

311   The D_{pm} sensitivity plots (Fig. 7) show a number of well-defined responses of D_{pm} to the inputs.

312   D_{pm} increases monotonically with increases in mass flux and fire area (Fig. 5b,d), and decreases nearly

313   monotonically with wind speed. These trends are due to the interrelationships of these inputs with

314   starting number concentration. These results are consistent with Fig. 4 and Fig. 5, where D_{pm} increased

315   with increasing dM/dx in the SAM-TOMAS simulations. Additionally, the D_{pm} also decreases

316   monotonically with mixing depth (albeit more weakly than mass flux, fire area, and wind speed), so

317   dM/dxdz may also be a good proxy for biomass-burning size-distribution aging (evaluated in Sect. 3.4).

318   Higher dM/dx and dM/dxdz values lead to higher initial number concentration in these plumes, which

319   drive higher rates of coagulation due the squared dependence of coagulation rate on number

320   concentrations.

321   D_{pm} also increases nearly monotonically with time (the regions of slight decreases with time

322   show that the parameterization is not necessarily always physically representative due to the statistical

323   nature of the fit over the parameter space). The rapid rise in D_{pm} for time <2 hrs is due to the high

324   number concentrations (N) and coagulation rates near the source. As dilution and coagulation progress,

325   N decreases and coagulation slows, resulting in a slowing of D_{pm} increase. Mass flux has the largest

326   range of output D_{pm} associated with the input ranges specified here (~ -50% to +100%).

327   The relationship between D_{pm} and the initial size parameters (D_{pm0} and σ_0) is more complicated.

328   Neither D_{pm0} nor σ_0 show monotonic increases or decreases in D_{pm} due to changes in either of these

329   isolated inputs. In general, there is an increasing trend in output D_{pm} with increasing D_{pm0}, but for some

330   cases it decreases. These decreases in D_{pm} are likely due to (1) decreasing particle number

331   concentrations with increasing D_{pm0}, which leads to reduced coagulation rates and (2) imperfections in

332   the statistical fit of the parameter space. The larger σ_0 indicate broader emission size distributions, with

333   more large particles and small particles. Since coagulation progresses fastest between large and small

334   particles (as opposed to particles of approximately the same size), this favors higher D_{pm} at higher σ.

335   However, the initial particle number decreases with increasing σ, which lowers the coagulation rate and

336   leads to lower D_{pm}.

337   The emulator-derived σ sensitivities are shown in Fig. 8. Since we expect σ to converge towards

338   an asymptotic limit with coagulational processing (Fig. 4b,d), we see with those input parameters

339   associated with higher plume number density (mass flux, fire area, wind speed^{-1}, mixing depth^{-1}), which

340   gave monotonic increases for D_{pm}, show mixed results for σ due to variability in the initial σ_0. The time

341   sensitivity plot (Fig. 8f) shows decreasing σ with time similar to Fig. 4b,d.

342   Emission σ_0 shows the most pronounced and largest magnitude effect on output σ (~ -30% to

343   +30%). Thus, the timescales for σ evolving towards 1.2 is longer than the timescales tested here for

344   even the densest plumes. These sensitivity plots show that there is less variability in σ than in D_{pm} over

345   the tested input space.

346   *3.4 Simplified fits to the aged size distributions*

347   In addition to the GEM-SA emulator fits, we determined simplified fits for both D_{pm} and σ based on the

348   behavior in Fig. 4 and Fig. 5. These fits are easier to implement in regional and global aerosol models

349   than the full GEM-derived parameterization. These equations are meant to produce approximate

350 estimates of D_{pm} and σ throughout plume size-distribution aging. The equations require: the initial

351 value of the size-parameter of interest (D_{pm0} or σ_0), a value proportional to the plume aerosol loading

352 (dM/dxdz: mass flux · fire area / wind speed / mixing depth or dM/dx: mass flux · fire area / wind

353 speed), and time since emission from the source fire (time). (Distance may also be used in these

354 equations rather than time, and distance/wind-speed should be used in place of time.) The functional

355 forms fitted for D_{pm} and σ are found below.

$$D_{pm} = D_{pm0} + A\,[dM/dx]^b\,(time)^c \tag{1}$$

$$D_{pm} = D_{pm0} + A\,[dM/dxdz]^b\,(time)^c \tag{2}$$

$$\sigma = \sigma_0 + A\,[dM/dx]^b\,(time)^c\,(1.2 - \sigma_0) \tag{3}$$

$$\sigma = \sigma_0 + A\,[dM/dxdz]^b\,(time)^c\,(1.2 - \sigma_0) \tag{4}$$

356

357 where A, b and c are determined by fitting each equation to the SAM-TOMAS data. For these

358 empirical equations, the units of dM/dx are kg m^{-1}, dM/dxdz are kg m^{-2}, D_{pm} is nm and time since

359 emission is min. It should be noted that the equations for D_{pm} and σ are designed to be independent of

360 each other (i.e. D_{pm} is not dependent on σ_0), which differs from the GEM-SA emulator. The aerosol

361 loading parameter dM/dx was chosen based on the stratification seen in Fig. 4c and Fig. 5. dM/dxdz

362 was tested as well, as it incorporates the variance associated with mixing depth into the fit. The fit to

363 dM/dx rather than dM/dxdz may be advantageous because we expect mixing depth of the plume to be

364 one of the more uncertain parameters in an atmospheric model, and the D_{pm} sensitivities to mixing

365 depth tend to be smaller than those to mass flux, fire area and wind speed in the GEM-SA emulator

366 (Fig. 7). The σ fits introduce a fourth factor, $(1.2 - \sigma_0)$, which represents the difference between the

367 SAM-TOMAS infinite-coagulation limit (Fig. 4b and d) and the initial modal width.

368   The scalar A, b and c variables were fit to the ensemble of SAM-TOMAS data. Their values are

369 summarized in Table 3. The fits were tested against independent SAM-TOMAS data in Fig. 9 (D_{pm}) and

370 Fig. 10 (σ). The simplified D_{pm} parameterizations, as expected, are not as good a fit of the

371 SAM-TOMAS data as the GEM-SA emulator (Fig. 6). The fit statistics for the simple

372 parameterizations are as follows: D_{pm}(dM/dx): slope = 0.82, R^2 = 0.67, MNB= 0.003, D_{pm}(dM/dxdz):

373 slope = 0.98, R^2 = 0.77, MNB= 0.008. The fit using dM/dxdz generally performs better than that with

374   dM/dx. The simple σ fit also did not perform as well as the GEM-SA emulator with fit statistics of:

375   σ(dM/dx): slope = 0.71, R^2= 0.75, MNB= 0.07 and, σ(dM/dxdz): slope = 0.71, R^2 = 0.76, MNB= 0.07).

376   Thus, dM/dxdz fits do yield better results than dM/dx (in particular for D_{pm}); however, a user may

377   choose to use the dM/dx fit if the mixing depth is unknown. We note that these fits are only valid

378   within the parameter ranges shown in Table 1.

3.5 OA production/loss

379

380   One of the limitations of the coagulation-only parameterizations derived in this paper is that they do not

381   include the effects of potential condensation/evaporation of organic aerosol on the aged

382   biomass-burning size distribution. Both condensational growth and evaporative loss of OA been

383   observed previously in chamber studies and the field due to OA production or evaporation from

384   dilution/chemistry (Cubison et al., 2011; Hecobian et al., 2011; Hennigan et al., 2011; Grieshop et al.,

385   2009).

386   Here we present a simple correction to our coagulation-only parameterizations to account for

387   in-plume OA production/loss. Each parameterization presented in this paper may be corrected to

388   include OA production/evaporation using the corrections below. We assume that the OA production or

389   loss does not affect the coagulation rates or σ, but acts to increase the final D_{pm}. These assumptions are

390   imperfect as irreversible condensation (evaporation) increases (decreases) σ; however, σ is preserved

391   during condensation or evaporation of semi-volatile material (Pierce et al., 2011). Regardless, for the

392   relatively small amounts of OA condensation/evaporation considered here, the change in σ and

393   coagulation rates should be minor. For larger changes in OA mass (more than a factor of ~2) due to

394   production/loss, our simple correction will have uncertainties due to these assumptions. Our correction

395   to the final D_{pm} has the following form:

$$D_{pm\,w/OA\,prod/loss} = D_{pm\,w/o\,OA\,prod/loss} \cdot \left(\frac{OAMass_{w/OA\,prod/loss} + BCMass}{OAMass_{w/o\,OA\,prod/loss} + BCMass} \right)^{1/3} \tag{5}$$

396

397   where $D_{pm\,w/o\,OA\,prod/loss}$ is the final D_{pm} from the coagulation-only GEM-SA emulator parameterization,

398   the biomass-burning aerosol OA mass (with and without additional production or loss) is in kg (per

399   particle or volume of air) and the BC mass is in kg (per particle or volume of air). Thus, for a doubling

400 of OA due to SOA production (one of the larger enhancements found in Hennigan et al., 2011),

401 particles that contain negligible BC will grow in diameter by 26% above the coagulation-only

402 predictions. If the particles contained 50% BC, then the diameter growth would only be 14%.

403   While these changes are expected to be on the large end for growth by SOA production, they

404 are significantly smaller than the ~200% variability in aged D_{pm} due to coagulation over the range of

405 initial fire conditions (Fig. 7). For example, variations in wind speed, mass flux, and fire area alone can

406 independently cause variability in the aged D_{pm} by a factor of 2 due to changes in coagulation rates

407 while variability in condensational growth appears to cause much smaller uncertainties (~25%) in the

408 aged D_{pm}. This indicates that although SOA condensational growth is certainly important in shaping

409 particle composition and total particle mass, it is not among the most dominant factors determining the

410 aged D_{pm} compared to those fire-condition parameters controlling coagulational growth. It should be

411 noted, however, that the D_{pm} growth attributed to OA condensation is not accompanied by a change in

412 particle number (additional OA mass is distributed among existing particles), whereas a similar

413 increase in D_{pm} growth by coagulation only would have an accompanying decrease in particle number.

414 Thus, the climatic influence of a size change due to coagulation and condensation are different.

4. Conclusions

416 We used the SAM-TOMAS large-eddy simulation model and an emulation technique to explore the

417 evolution of biomass-burning aerosol size distributions due to coagulation and build coagulation-only

418 parameterizations of this size-distribution evolution. We have also provided a simple correction to the

419 parameterization for cases with net OA production or loss. We used the SAM-TOMAS model to

420 simulate plume dispersion and aerosol coagulation. The SAM-TOMAS results show that the aged D_{pm}

421 can be largely described by dM/dx and the distance from the source (or time since emission). These

422 results also show that the aged σ moves from σ_0 towards a value of 1.2 at a rate that depends on dM/dx.

423   The GEM-SA program was used to derive a D_{pm} and σ emulator parameterization based on the

424 SAM-TOMAS results. The parameterization requires seven input parameters: emission D_{pm0}, emission

425 σ_0, mass flux, boundary layer wind speed, fire area, plume mixing depth, and time since emission. The

426 predicted D_{pm} and σ can then be used as effective unimodal biomass-burning size-distribution

427 parameters in regional and global aerosol models.

428   The D_{pm} parameterization showed the strongest sensitivities to those input parameters associated

429   with the extent of aerosol loading within the plume (mass flux, fire area, wind speed). Across the fire

430   area and wind speed ranges tested here, final D_{pm} varied by ± 50%. Mass flux had the largest associated

431   D_{pm} sensitivity across the tested values (-50% to +100%). These sensitivities were larger than those

432   associated with mixing depth (~ -20% to 20%) or the initial size-distribution parameters (D_{pm0}: ~ -25%

433   to 25%, σ_0: ~ 15% to -15%). The σ parameterization showed a uniform decrease in σ with time and

434   strong sensitivities to the emission σ_0 (-30% to 30%). This strong sensitivity to σ_0 can be attributed to

435   the inertia in σ evolution in simulations with large modal widths and relatively small mass loading,

436   where σ will not converge quickly to the coagulational limit (1.2).

437   The GEM-SA-derived parameterization performed relatively well against the SAM-TOMAS

438   model with a correlation of R^2=0.83, slope of m=0.92 and a low mean normalized bias of MNB=-0.06

439   for D_{pm}. The σ parameterization has fit statistics of R^2= 0.93, slope= 0.91 and MNB= 0.01. The σ

440   parameterization was unable to capture the coagulational limit of 1.2 seen in the SAM-TOMAS results

441   and instead extrapolated to lower values. This 1.2 limit differs from the 1.32 σ limit proposed by Lee

442   (1983) due to the bin-spacing in SAM-TOMAS being coarser than lognormal modes with these small

443   modal widths.

444   We also provided simplified polynomial fits for D_{pm} and σ (Eqns 1-4, Table 3) for calculating

445   aged D_{pm} and σ as independent functions of: the fresh emission parameter (D_{pm0} or σ_0), the mass loading

446   of the aerosol (dM/dx or dM/dxdz) and the time since emission from the source fire. The σ fits also

447   require a convergence term to account for the coagulational limit (1.2 in the SAM-TOMAS model).

448   Tested against independent SAM-TOMAS data, the D_{pm} simplified fits performed as: D_{pm}(dM/dx):

449   slope = 0.82, R^2 = 0.67, MNB= 0.003 and D_{pm}(dM/dxdz): slope = 0.98, R^2 = 0.77, MNB= 0.008. The σ

450   simplified fits have statistics of σ(dM/dx): slope = 0.71, R^2= 0.75, MNB= 0.07 and σ(dM/dxdz): slope

451   = 0.71, R^2 = 0.76, MNB= 0.07. The equations requiring (dM/dxdz) performed better than their (dM/dx)

452   counterparts as they also account for the aerosol layer depth.

453   We provided a correction for OA production/loss, and showed that significant production of

454   SOA within the plume (~ 100% OA mass enhancement) would cause a relatively small shift in the

455   size-distribution D_{pm} (14-26% increase) compared to other factors that control the coagulation rate (e.g.

456   dM/dx). Thus, variability in factors controlling coagulation may cause more variability in the aged

457   biomass-burning particle size than variability in SOA production. We note, however, that OA

458   production increases D_{pm} without loss of particle number while coagulation increases D_{pm} with a

459   decrease in number, thus the climatic impact of condensation and coagulation are different. The

460   simplified OA-production/loss correction assumes no change in σ with condensational growth. Further

461   testing should be done with explicit OA production and loss to better quantify the effects of

462   condensation of the size-distribution evolution.

463   Our analysis does not include any cloud processing of the plume particles, i.e. the production of

464   aqueous SOA within activated plume particles is not accounted for in our simple OA mass correction.

465   The production of SOA within droplets could result in additional SOA mass being only added to the

466   larger, activated particles during activation/evaporation cycling. This extra SOA mass would favor

467   increases in the diameters of the larger particles of the size-distribution only, which could create a

468   bimodal size distribution and increase the overall coagulational rates in the plume (more, larger

469   particles coagulate more rapidly with the small-diameter particles).

470   Future work includes (1) testing the parameterizations developed in this work against real world

471   observations of size distribution aging, and (2) incorporating the parameterizations into regional and

472   global aerosol models for further evaluation against regional/global measurements.

473

474   5. Author Contribution

475   K.M. Sakamoto, R.G. Stevens, and J.R. Pierce designed the study. K. M. Sakamoto performed the

476   SAM-TOMAS simulations, and created and evaluated the parameterizations. K. M. Sakamoto prepared

477   the manuscript with assistance from all co-authors.

478   6. Acknowledgements

479   NCEP Reanalysis data provided by the NOAA/OAR/ESRL PSD, Boulder, Colorado, USA, from their

480   Web site at http://www.esrl.noaa.gov/psd/. K.M. Sakamoto was funded by a Natural Sciences and

481   Engineering Research Council of Canada (NSERC) PGS-M Fellowship.

482

483   7. References

484   Adams, P. J. and Seinfeld, J. H.: Predicting global aerosol size distributions in general circulation

485   models, Journal of Geophysical Research-Atmospheres, 107, 4310 - 4370, 2002.

486   Adler, G., Flores, J. M., Abo Riziq, A., Borrmann, S. and Rudich, Y.: Chemical, physical, and optical
487   evolution of biomass burning aerosols: a case study, Atmos. Chem. Phys., 11(4), 1491–1503,
488   doi:10.5194/acp-11-1491-2011, 2011.

489   Alonso-Blanco, E., Calvo, A. I., Pont, V., Mallet, M., Fraile, R. and Castro, A. Impact of Biomass
490   Burning on Aerosol Size Distribution, Aerosol Optical Properties and Associated Radiative
491   Forcing, Aerosol Air Qual. Res., 006, 708–724, doi:10.4209/aaqr.2013.05.0163, 2014.

492   Andreae, M. O. and Merlet, P.: Emission of trace gases and aerosols from biomass burning, Global
493   Biogeochem. Cycles, 15(4), 955–966, doi:10.1029/2000GB001382, 2001.

494   Boucher, O., Randall, D., Artaxo, P., Bretherton, C., Feingold, G., Forster, P., Kerminen, V.-M., Kondo,
495   Y., Liao, H., Lohmann, U., Rasch, P., Satheesh, S. K., Sherwood, S., Stevens, B. & Zhang, X. Y.
496   in *Climate Change 2013: The Physical Science Basis. Contribution of Working Group I to the*
497   *Fifth Assessment Report of the Intergovernmental Panel on Climate Change* (eds. Stocker, T. F.
498   et al.) (Cambridge University Press, 2013).

499   Capes, G., Johnson, B., McFiggans, G., Williams, P. I., Haywood, J., and Coe, H.: Aging of biomass
500   burning aerosols over West Africa: Aircraft measurements of chemical composition, microphysical
501   properties, and emission ratios, Journal of Geophysical Research, 113, D00C15,
502   doi:10.1029/2008JD009845, 2008.

503   Carrico, C. M., Petters, M. D., Kreidenweis, S. M., Sullivan, A. P., McMeeking, G. R., Levin, E. J. T.,
504   Engling, G., Malm, W. C. and Collett, J. L.: Water uptake and chemical composition of fresh
505   aerosols generated in open burning of biomass, Atmos. Chem. Phys., 10(11), 5165–5178,
506   doi:10.5194/acp-10-5165-2010, 2010.

507   Carslaw, K. S., Lee, L. A., Reddington, C. L., Pringle, K. J., Rap, A., Forster, P. M., Mann, G. W.,
508   Spracklen, D. V, Woodhouse, M. T., Regayre, L. A. and Pierce, J. R.: Large contribution of natural
509   aerosols to uncertainty in indirect forcing, Nature, 503(7474), 67–71 doi:10.1038/nature12674,
510   2013.

511   Cubison, M. J., Ortega, a. M., Hayes, P. L., Farmer, D. K., Day, D., Lechner, M. J., Brune, W. H., Apel,
512   E., Diskin, G. S., Fisher, J. a., Fuelberg, H. E., Hecobian, a., Knapp, D. J., Mikoviny, T., Riemer,
513   D., Sachse, G. W., Sessions, W., Weber, R. J., Weinheimer, A. J., Wisthaler, a., and Jimenez, J. L.:
514   Effects of aging on organic aerosol from open biomass burning smoke in aircraft and laboratory
515   studies, Atmospheric Chemistry and Physics, 11, 12 049-12 064, doi:10.5194/acp-11-12049-2011,
516   2011.

517   DeCarlo, P. F., Ulbrich, I. M., Crounse, J., de Foy, B., Dunlea, E. J., Aiken, A. C., Knapp, D.,
518   Weinheimer, A. J., Campos, T., Wennberg, P. O. and Jimenez, J. L.: Investigation of the sources
519   and processing of organic aerosol over the Central Mexican Plateau from aircraft measurements
520   during MILAGRO, Atmos. Chem. Phys., 10(12), 5257–5280, doi:10.5194/acp-10-5257-2010,
521   2010.

522   Engelhart, G. J., Hennigan, C. J., Miracolo, M. A., Robinson, A. L. and Pandis, S. N.: Cloud
523   condensation nuclei activity of fresh primary and aged biomass burning aerosol, Atmos. Chem.
524   Phys., 12(15), 7285–7293, doi:10.5194/acp-12-7285-2012, 2012.

525   Freitas, S. R., Longo, K. M., Chatfield, R., Latham, D., Dias, M. A. F. S., Andreae, M. O., Prins, E.,
526   and Unesp, F. E. G.: Including the sub-grid scale plume rise of vegetation fires in low resolution
527   atmospheric transport models, Atmospheric Chemistry and Physics, pp. 3385 - 3398, 2007.

528 Grieshop, A. P., Logue, J. M., Donahue, N. M. and Robinson, A. L.: Laboratory investigation of
529 photochemical oxidation of organic aerosol from wood fires 1: measurement and simulation of
530 organic aerosol evolution, Atmos. Chem. Phys., 9(4), 1263–1277, doi:10.5194/acp-9-1263-2009,
531 2009.

532 Haywood, J. and Boucher, O.: Estimates of the direct and indirect radiative forcing due to tropospheric
533 aerosols: a review, Rev. Geophys., 38, 513–543, doi:10.1029/1999RG000078, 2000.

534 Hecobian, A., Liu, Z., Hennigan, C. J., Huey, L. G., Jimenez, J. L., Cubison, M. J., Vay, S., Diskin, G.
535 S., Sachse, G. W., Wisthaler, A., Mikoviny, T., Weinheimer, A. J., Liao, J., Knapp, D. J.,
536 Wennberg, P. O., Kürten, A., Crounse, J. D., Clair, J. St., Wang, Y. and Weber, R. J.: Comparison
537 of chemical characteristics of 495 biomass burning plumes intercepted by the NASA DC-8 aircraft
538 during the ARCTAS/CARB-2008 field campaign, Atmos. Chem. Phys., 11(24), 13325–13337,
539 doi:10.5194/acp-11-13325-2011, 2011.

540 Hennigan, C. J., Miracolo, M. A., Engelhart, G. J., May, A. A., Presto, A. A., Lee, T., Sullivan, A. P.,
541 McMeeking, G. R., Coe, H., Wold, C. E., Hao, W.-M., Gilman, J. B., Kuster, W. C., de Gouw, J.,
542 Schichtel, B. A., Kreidenweis, S. M. and Robinson, A. L.: Chemical and physical transformations
543 of organic aerosol from the photo-oxidation of open biomass burning emissions in an
544 environmental chamber, Atmos. Chem. Phys., 11(15), 7669–7686, doi:10.5194/acp-11-7669-2011,
545 2011.

546 Hennigan, C. J., Westervelt, D. M., Riipinen, I., Engelhart, G. J., Lee, T., Collett, J. L., Pandis, S. N.,
547 Adams, P. J. and Robinson, A. L.: New particle formation and growth in biomass burning plumes:
548 An important source of cloud condensation nuclei, Geophys. Res. Lett., 39(9), n/a–n/a,
549 doi:10.1029/2012GL050930, 2012.

550 Heringa, M. F., DeCarlo, P. F., Chirico, R., Tritscher, T., Dommen, J., Weingartner, E., Richter, R.,
551 Wehrle, G., Prévôt, A. S. H. and Baltensperger, U.: Investigations of primary and secondary
552 particulate matter of different wood combustion appliances with a high-resolution time-of-flight
553 aerosol mass spectrometer, Atmos. Chem. Phys., 11(12), 5945–5957,
554 doi:10.5194/acp-11-5945-2011, 2011.

555 Hobbs, P. V., Sinha, P., Yokelson, R. J., Christian, T. J., Blake, D. R., Gao, S., Kirchstetter, T. W.,
556 Novakov, T. and Pilewskie, P.: Evolution of gases and particles from a savanna fire in South
557 Africa, J. Geophys. Res., 108(D13), doi:10.1029/2002JD002352, 2003.

558 Hosseini, S., Li, Q., Cocker, D., Weise, D., Miller, A., Shrivastava, M., Miller, J. W., Mahalingam, S.,
559 Princevac, M. and Jung, H.: Particle size distributions from laboratory-scale biomass fires using
560 fast response instruments, Atmos. Chem. Phys., 10(16), 8065–8076,
561 doi:10.5194/acp-10-8065-2010, 2010.

562 Huffman, J. A., Docherty, K. S., Mohr, C., Cubison, M. J., Ulbrich, I. M., Ziemann, P. J., Onasch, T. B.
563 and Jimenez, J. L.: Chemically-Resolved Volatility Measurements of Organic Aerosol from
564 Different Sources, Environ. Sci. Technol., 43(14), 5351–5357, doi:10.1021/es803539d, 2009.

565 Jacobson, M. Z.: Strong radiative heating due to the mixing state of black carbon in atmospheric
566 aerosols, Nature, 409(6821), 695–697, 2001.

567 Janhäll, S., Andreae, M. O. and Pöschl, U.: Biomass burning aerosol emissions from vegetation fires :
568 particle number and mass emission factors and size distributions, Atmos. Chem. Phys, 1427–1439,
569 2010.

570 Kennedy, M. and O'Hagan, A.: Bayesian calibration of computer models, J. R. Stat. Soc. Ser. B Stat.

571   Methodol., 63, 425 - 464, 2001.

572   Kennedy, M., Anderson, C., O'Hagan, A., Lomas, M., Woodward, I., Gosling, J. P., and Heinemeyer,A.:
573   Quantifying uncertainty in the biospheric carbon flux for England and Wales, Journal of the Royal
574   Statistical Society: Series A (Statistics in Society), 171, 109-135,
575   doi:10.1111/j.1467-985X.2007.00489.x, 2008.

576   Khairoutdinov, M. F. and Randall, D. A.: Cloud resolving modeling of the ARM summer 1997 IOP:
577   Model formulation, results, uncertainties, and sensitivities, Journal of the Atmospheric Sciences,
578   60, 607-625, 2003.

579   Lee, K.: Change of particle size distribution during Brownian coagulation, Journal of Colloid and
580   Interface Science, 92, 315 - 325, doi:http://dx.doi.org/10.1016/0021-9797(83)90153-4, 1983.

581   Lee, L. A., Carslaw, K. S., Pringle, K. J., Mann, G. W., and Spracklen, D. V.: Emulation of a complex
582   global aerosol model to quantify sensitivity to uncertain parameters, Atmospheric Chemistry and
583   Physics, 11, 12 253{12 273, doi:10.5194/acp-11-12253-2011, 2011.

584   Lee, L. A., Carslaw, K. S., Pringle, K. J., and Mann, G. W.: Mapping the uncertainty in global CCN
585   using emulation, Atmospheric Chemistry and Physics, 12, 9739 – 9751,
586   doi:10.5194/acp-12-9739-2012, 2012.

587   Lee, L. A., Pringle, K. J., Reddington, C. L., Mann, G. W., Stier, P., Spracklen, D. V., Pierce, J. R., and
588   Carslaw, K. S.: The magnitude and causes of uncertainty in global model simulations of cloud
589   condensation nuclei, Atmospheric Chemistry and Physics, 13, 8879-8914,
590   doi:10.5194/acp-13-8879-2013, 2013.

591   Levin, E. J. T., McMeeking, G. R., Carrico, C. M., Mack, L. E., Kreidenweis, S. M., Wold, C. E.,
592   Moosmüller, H., Arnott, W. P., Hao, W. M., Collett, J. L. and Malm, W. C.: Biomass burning
593   smoke aerosol properties measured during Fire Laboratory at Missoula Experiments (FLAME), J.
594   Geophys. Res., 115(D18), D18210, doi:10.1029/2009JD013601, 2010.

595   Lonsdale, C. R., Stevens, R. G., Brock, C. a., Makar, P. a., Knipping, E. M., and Pierce, J. R.: The
596   effect of coal-powered power-plant SO_2 and NO_x control technologies on aerosol nucleation in the
597   source plumes, Atmospheric Chemistry and Physics, 12, 11 519-11 531,
598   doi:10.5194/acp-12-11519-2012, 2012.

599   May, A. A., Levin, E. J. T., Hennigan, C. J., Riipinen, I., Lee, T., Collett, J. L., Jimenez, J. L.,
600   Kreidenweis, S. M. and Robinson, A. L.: Gas-particle partitioning of primary organic aerosol
601   emissions: 3. Biomass burning, J. Geophys. Res. Atmos., 118(19), 11,327–11,338,
602   doi:10.1002/jgrd.50828, 2013.

603   Mesinger, F., Dimego, G., Kalnay, E., Mitchell, K., Shafran, P. C., Ebisuzaki, W., Jovi□, D., Woollen,
604   J., Rogers, E., Berbery, E. H., Ek, M. B., Fan, Y., Grumbine, R., Higgins, W., Li, H., Lin, Y.,
605   Manikin, G., Parrish, D., and Shi, W.: North American Regional Reanalysis: A long-term,
606   consistent, high-resolution climate dataset for the North American domain, as a major
607   improvement upon the earlier global reanalysis datasets in both resolutionand accuracy, B. Am.
608   Meteorol. Soc., 87, 343–360, 2006.

609   Okoshi, R., Rasheed, A., Chen Reddy, G., McCrowey, C. J. and Curtis, D. B.: Size and mass
610   distributions of ground-level sub-micrometer biomass burning aerosol from small wildfires,
611   Atmos. Environ., 89, 392–402, doi:10.1016/j.atmosenv.2014.01.024, 2014.

612   Ortega, A. M., Day, D. A., Cubison, M. J., Brune, W. H., Bon, D., de Gouw, J. A. and Jimenez, J. L.:
613   Secondary organic aerosol formation and primary organic aerosol oxidation from biomass-burning
614   smoke in a flow reactor during FLAME-3, Atmos. Chem. Phys., 13(22), 11551–11571,

615   doi:10.5194/acp-13-11551-2013, 2013.

616 Petters, M. D. and Kreidenweis, S. M.: A single parameter representation of hygroscopic growth and
617   cloud condensation nucleus activity, Atmos. Chem. Phys., 7(8), 1961–1971,
618   doi:10.5194/acp-7-1961-2007, 2007.

619 Petters, M. D., Carrico, C. M., Kreidenweis, S. M., Prenni, A. J., DeMott, P. J., Collett, J. L. and
620   Moosmüller, H.: Cloud condensation nucleation activity of biomass burning aerosol, J. Geophys.
621   Res., 114(D22), D22205, doi:10.1029/2009JD012353, 2009.

622 Pierce, J. R., Chen, K. and Adams, P. J.: Contribution of primary carbonaceous aerosol to cloud
623   condensation nuclei: processes and uncertainties evaluated with a global aerosol microphysics
624   model, Atmos. Chem. Phys., 7, 5447–5466, 2007.

625 Pierce, J.R., Riipinen, I., Kulmala, M., Ehn, Petaja, T., Junninen, H., Worsnop, D.R., Donahue, N.M.:
626   Quantification of the volatility of secondary organic compounds in ultrafine particles during
627   nucleation events, Atmospheric Chemistry and Physics, 11, 9019-9036,
628   doi:10.5194/acp-11-9019-2011, 2011.

629 Reid, J. S., Koppmann, R., Eck, T. F. and Eleuterio, D. P.: A review of biomass burning emissions part
630   II: intensive physical properties of biomass burning particles, Atmos. Chem. Phys., 5(3), 799–825,
631   doi:10.5194/acp-5-799-2005, 2005.

632 Rissler, J., Vestin, A., Swietlicki, E., Fisch, G., Zhou, J., Artaxo, P. and Andreae, M. O.: Size
633   distribution and hygroscopic properties of aerosol particles from dry-season biomass burning in
634   Amazonia, Atmos. Chem. Phys., 6, 471–491, 2006.

635 Sakamoto, K. M., Allan, J. D., Coe, H., Taylor, J. W., Duck, T. J., and Pierce, J. R.: Aged boreal
636   biomass-burning aerosol size distributions from BORTAS 2011, Atmos. Chem. Phys., 15,
637   1633-1646, doi:10.5194/acp-15-1633-2015, 2015.

638 Seinfeld, J. H. and Pandis, S. N.: Atmospheric Chemistry and Physics, Wiley, 2006.

639 Spracklen, D. V., Carslaw, K. S., Pöschl, U., Rap, A. and Forster, P. M.: Global cloud condensation
640   nuclei influenced by carbonaceous combustion aerosol, Atmos. Chem. Phys., 11(17), 9067–9087,
641   doi:10.5194/acp-11-9067-2011, 2011.

642 Stevens, R. G. and Pierce, J. R.: A parameterization of sub-grid particle formation in sulfur-rich plumes
643   for global- and regional-scale models, Atmospheric Chemistry and Physics, 13, 12 117-12 133,
644   doi:10.5194/acp-13-12117-2013, 2013.

645 Stevens, R. G. and Pierce, J. R.: The contribution of plume-scale nucleation to global and regional
646   aerosol and CCN concentrations: evaluation and sensitivity to emissions changes, Atmospheric
647   Chemistry and Physics Discussions, 14, 21 473 - 21 521, doi:10.5194/acpd-14-21473-2014, 2014.

648 Stevens, R. G., Pierce, J. R., Brock, C. A., Reed, M. K., Crawford, J. H., Holloway, J. S., Ryerson, T.
649   B., Huey, L. G., and Nowak, J. B.: Nucleation and growth of sulfate aerosol in coal-powered
650   power plant plumes: sensitivity to background aerosol and meteorology, Atmospheric Chemistry
651   and Physics, 12, 189 - 206, doi:10.5194/acp-12-189-2012, 2012.

652 Stuart, G. S., Stevens, R. G., a. I. Partanen, Jenkins, a. K. L., Korhonen, H., Forster, P. M., Spracklen,
653   D. V., and Pierce, J. R.: Reduced efficacy of marine cloud brightening geoengineering due to
654   in-plume aerosol coagulation: parameterization and global implications, Atmospheric Chemistry
655   and Physics, 13, 10 385-10 396, doi:10.5194/acp-13-10385-2013, 2013.

656 Van der Werf, G. R., Randerson, J. T., Giglio, L., Collatz, G. J., Mu, M., Kasibhatla, P. S., Morton, D.
657   C., DeFries, R. S., Jin, Y. and van Leeuwen, T. T.: Global fire emissions and the contribution of

658   deforestation, savanna, forest, agricultural, and peat fires (1997–2009), Atmos. Chem. Phys.,
659   10(23), 11707–11735, doi:10.5194/acp-10-11707-2010, 2010.

660 Whitby, E., McMurry, P., Shankar, U., and Binkowski, F. S.: Modal Aerosol Dynamics Modeling, Tech.
661   rep., Office of research and development U.S. environmental protection agency, 1991.

662 Wiedinmyer, C., Akagi, S. K., Yokelson, R. J., Emmons, L. K., Al-Saadi, J. A., Orlando, J. J. and Soja,
663   A. J.: The Fire INventory from NCAR (FINN): a high resolution global model to estimate the
664   emissions from open burning, Geosci. Model Dev., 4(3), 625–641, doi:10.5194/gmd-4-625-2011,
665   2011.

666 Yokelson, R. J., Crounse, J. D., Decarlo, P. F., Karl, T., Urbanski, S., Atlas, E., Campos, T. and
667   Shinozuka, Y.: Emissions from biomass burning in the Yucatan, Atmos. Chem. Phys., 5785–5812,
668   2009.

669

670

671 **Table 1.** Parameter ranges for each of the seven input parameters investigated in this study.

672

Parameter	Description	Units	Min. Value	Max. Value
D_{pm0}	Emission median dry diameter	nm	20	100
σ_0	Emission modal width	-	1.2	2.4
Mass Flux	Emission mass flux from fire	kg m^{-2} s^{-1}	2×10^{-8}	5×10^{-6}
Fire area	Square fire emissions area	km^2	1	49
Wind speed	Mean boundary-layer wind speed	m s^{-1}	2	20
Mixing depth	Mixing depth of aerosol layer	m	120	2500
Time	Time since emission	min	0	300

673
674
675
676
677
678
679
680
681
682
683
684
685
686
687
688
689
690
691
692
693
694
695
696
697
698
699
700
701
702

703   **Table 2.** Parameter ranges for inputs to the SAM-TOMAS model.
704

Parameter	Description	Units	Min. value	Max. value
Date	Req. for Met. field selection	8-hour	July 1, 2010	July 31, 2010
Latitude		deg N	30	70
Longitude		deg W	70	135
D_{pm0}	Emission median dry diameter	nm	20	100
σ_0	Emission modal width	-	1.2	2.4
Mass Flux	Emission mass flux from fire	kg m^{-2} s^{-1}	2×10^{-8}	5×10^{-6}
Fire area	Square fire emissions area	km^2	1	49
Injection height	Lower plume injection bound	m	50	150
Injection depth	Depth of plume at emission	m	500	2000

705
706
707
708
709

710

711
712
713
714
715
716
717
718
719
720
721
722
723
724
725
726
727

728 **Table 3.** Best-fit parameters for the simplified D_{pm} and σ SAM-TOMAS parameterizations (Eqns. 1 to
729 4)

Fit	Eqn. #	Parameter		
		A	b	c
$D_{pm}(dM/dx)$	(1)	4.268	0.3854	0.4915
$D_{pm}(dM/dxdz)$	(2)	84.58	0.4191	0.4870
$\sigma(dM/dx)$	(3)	0.05940	0.1915	0.3569
$\sigma(dM/dxdz)$	(4)	0.2390	0.1889	0.3540

730
731
732
733
734
735
736
737
738
739
740
741
742
743
744
745
746
747
748
749
750
751
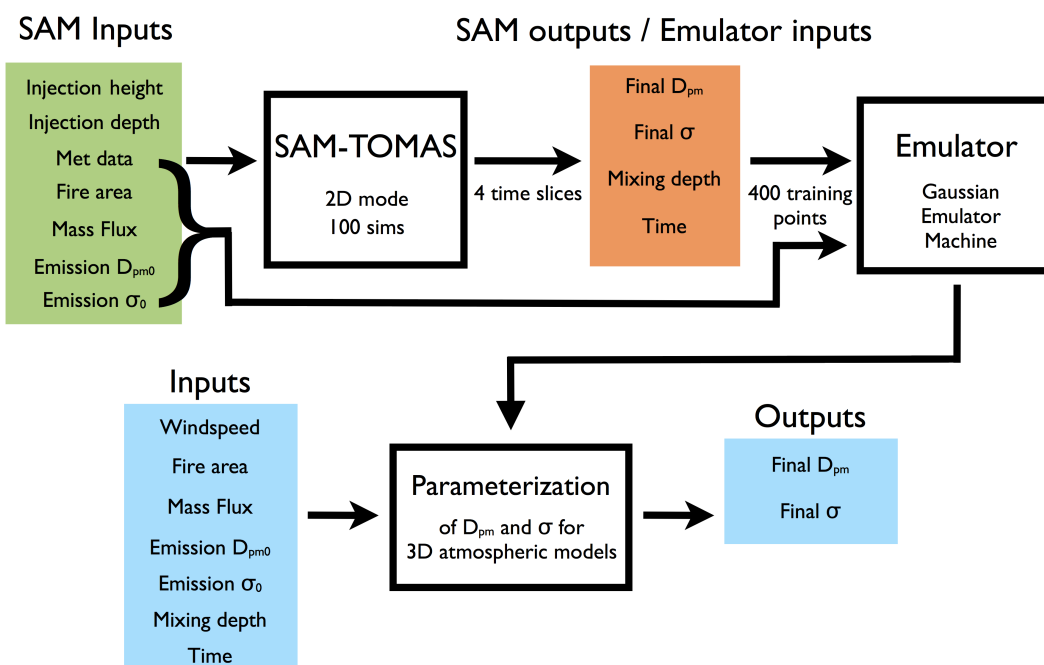
753
754
755 **Figure 1.** Schematic of the methods in this paper.

756
757
758
759
760
761
762
763
764
765
766
767
768
769
770
771
772
773
774
775
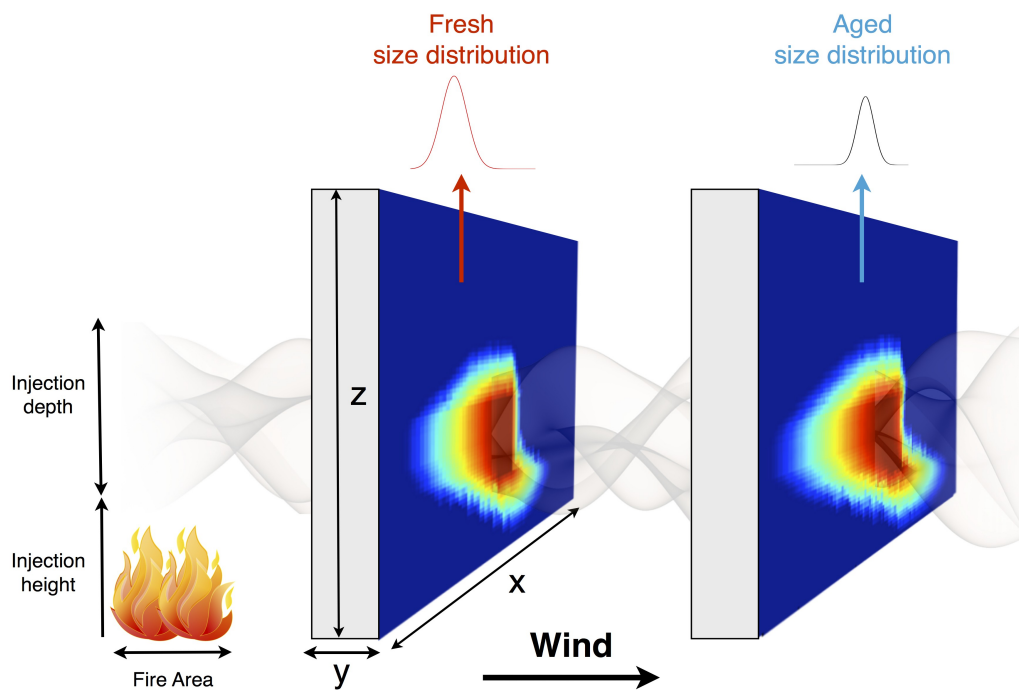
777
778
779   **Figure 2.** Schematic of a 2D SAM-TOMAS plume simulation.
780
781
782
783
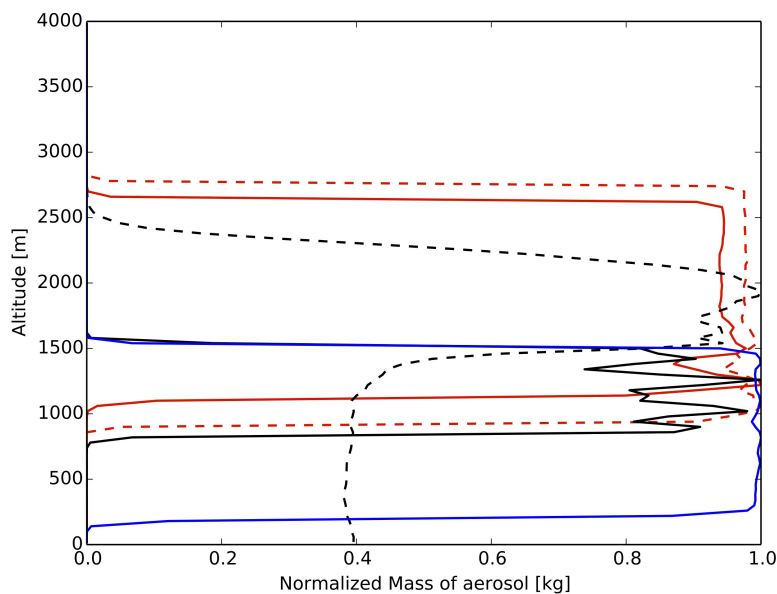
784
785
786
787
788
789
790
791
792
793
794
795
796
797
798
799
800

Figure 3. Final vertical profiles for five SAM-TOMAS simulations after four hours, normalized to individual aerosol load and averaged horizontally across the domain. The profiles show a variety of mixing depths, with some fully mixing through the boundary layer, while others are still stable at the emission injection layer.

846
847
848
849
850
851
852
853
854
855
856
857

858
859
860
861
862
863
864
865
866
867
868
869
870

Figure 4. Wire plots showing size-distribution changes across individual SAM-TOMAS simulations colored by emission mass flux (panels a and b) and dM/dx (panels c and d) for D_{pm} (panels a and c) and σ (panels b and d).

874
875
876
877
878
879
880
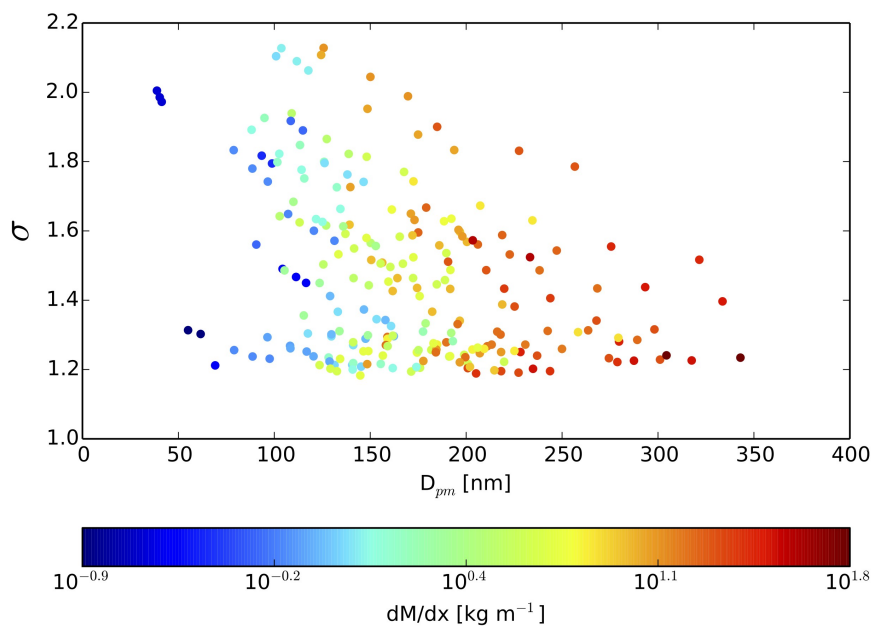
881 **Figure 5.** Scatter plot showing the relationships between final modal width (σ), final D_{pm}, and dM/dx

882 for each of the SAM-TOMAS simulation slices at distances greater than 25 km from the fire.

883

884

885
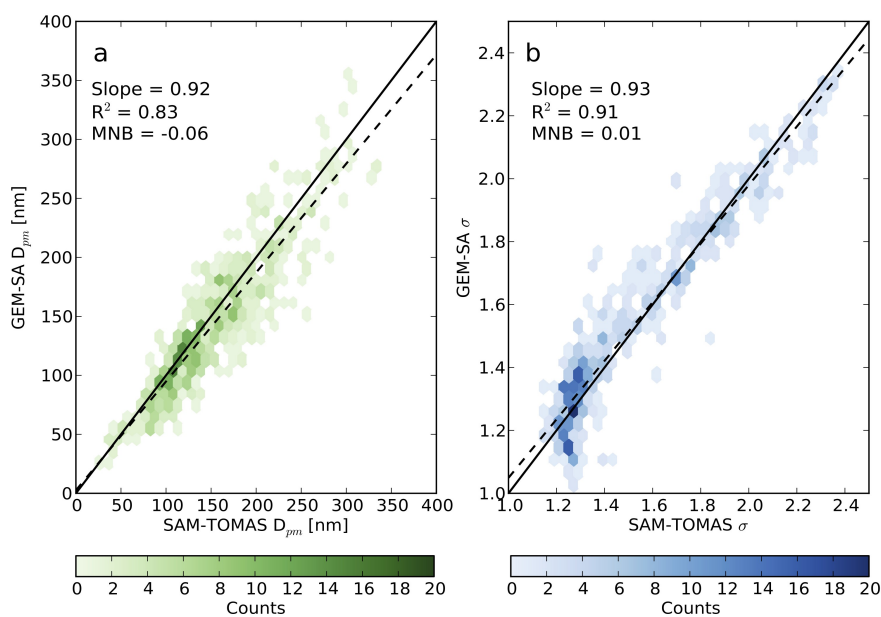
Figure 6. One-to-one plots showing GEM-SA emulator vs. SAM-TOMAS for 624 non-training simulation slices for a) final D_{pm}, and b) final modal width, σ. The black line is the one-to-one line. The dashed black line is the line of best fit.

886

887

888

889

890

891

892

893

894

895

896

897

898

899

900

901

902

903

904

905

906

907

908

909
910
911
912
913
914
915
916
917
918
919
920
921
922
923
924
925
926
927
928
929
930
931
932
933
934
935
936
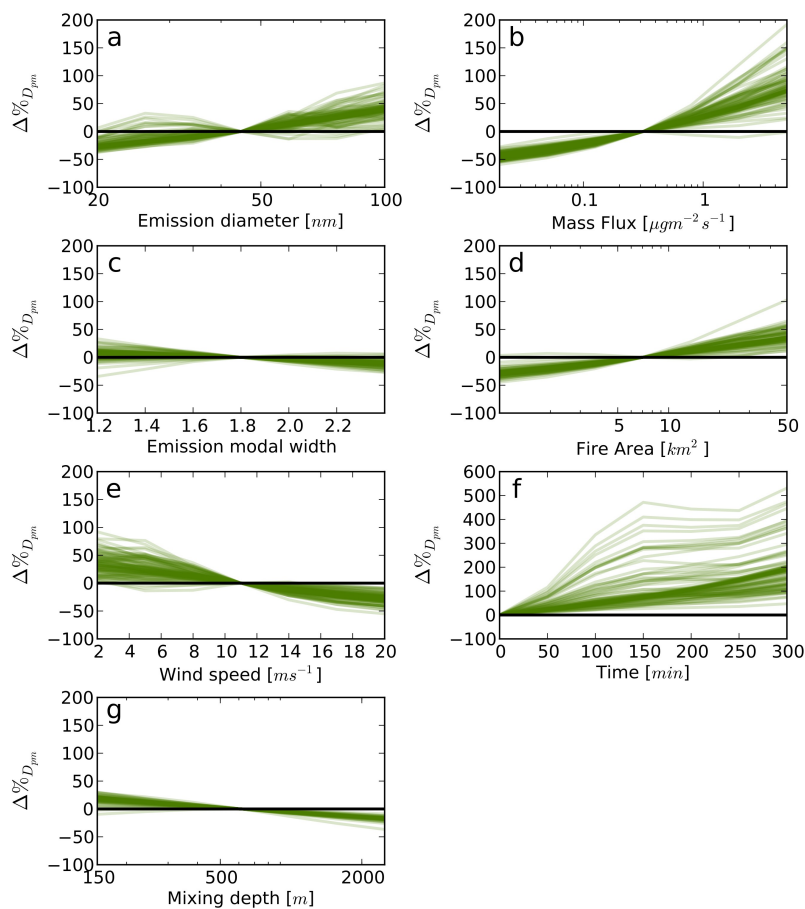
937 **Figure 7.** Sensitivity plots for the seven input parameters to the GEM-SA D_{pm} parameterization. For

938 each panel, a single input parameter is varied systematically from its minimum to maximum value for

939 100 randomly chosen sets of the other six parameters (100 lines in each panel). The sensitivities are

940 shown as percent change in final D_{pm}, individually normalized to the value at the center of the x-axis (to

941 zero in Time).

942

943
944
945
946
947
948
949
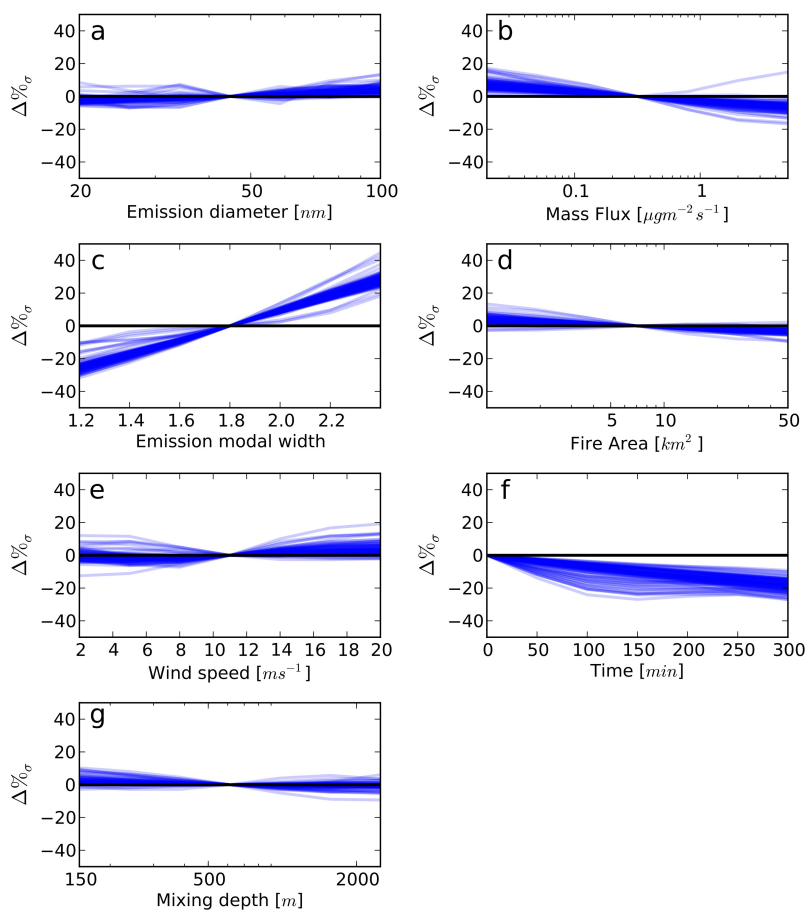
Figure 8. Sensitivity plots for the seven input parameters to the GEM-SA σ emulator parameterization. For each panel, a single input parameter is varied systematically from its minimum to maximum value for 100 randomly chosen sets of the other six parameters (100 lines in each panel). The sensitivities are shown as percent change in final σ, individually normalized to the center value of the x-axis (to zero in Time).
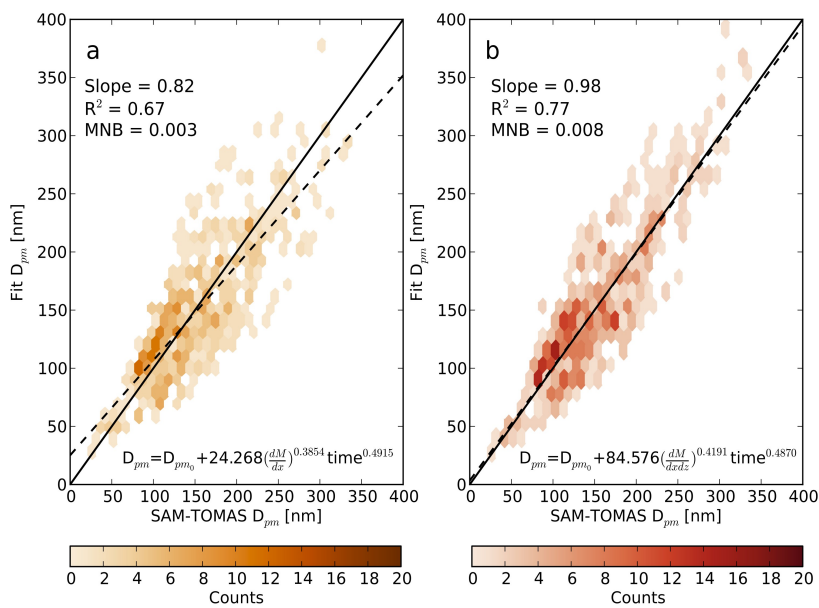
Figure 9. One-to-one plot showing simplified D_{pm} fits vs SAM-TOMAS for a) dM/dx, and b) dM/dxdz. The black line is the one-to-one line. The dashed black line is the line of best fit. N = 624.
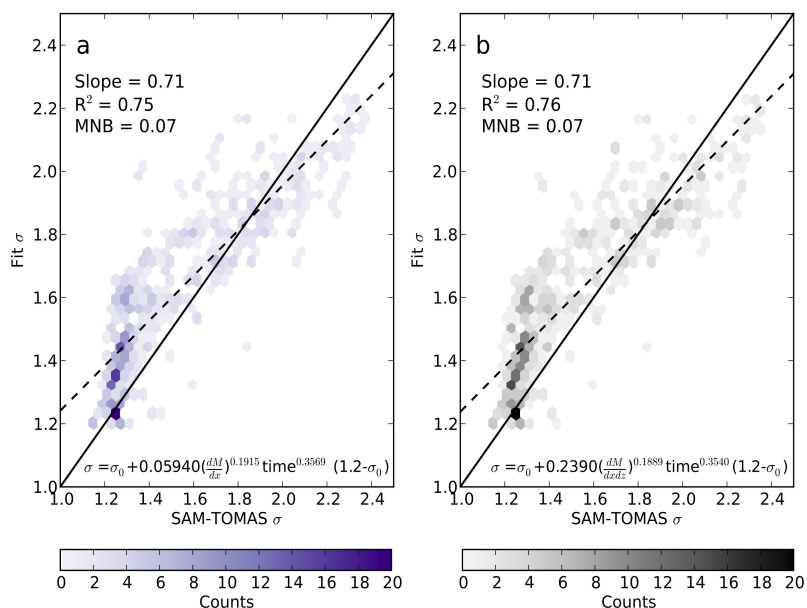
Figure 10. One-to-one plot showing simplified σ fits vs SAM-TOMAS for a) dM/dx, and b) dM/dxdz. The solid black line is the one-to-one line. The dashed black line is the line of best linear fit. N = 624.